Journal of Solid State Chemistry 184 (2011) 2446–2457

Contents lists available at ScienceDirect

Journal of Solid State Chemistry

journal homepage: www.elsevier.com/locate/jssc

Phonon properties of nanosized $MnWO_4$ with different size and morphology

Mirosław Mączka [a,*], Maciej Ptak [a], Michalina Kurnatowska [a], Leszek Kępiński [a], Paweł Tomaszewski [a], Jerzy Hanuza [a,b]

[a] Institute of Low Temperature and Structure Research, Polish Academy of Sciences, P.O. Box 1410, 50-950 Wrocław 2, Poland
[b] Department of Bioorganic Chemistry, Faculty of Industry and Economics, University of Economics, ul. Komandorska 118/120, 53-345 Wrocław, Poland

ARTICLE INFO

Article history:
Received 30 April 2011
Received in revised form
12 July 2011
Accepted 14 July 2011
Available online 22 July 2011

Keywords:
Hierarchical nanostructures
SEM
TEM
Infrared
Raman

ABSTRACT

Highly hierarchical barlike and flowerlike $MnWO_4$ microcrystals have been synthesized for the first time by a hydrothermal method, where ethanolamine (EA) and cetyltrimethylamonnium bromide (CTAB) play important roles in directing growth and self-assembly of these structures. The possible formation process has been proposed. In addition, platelike nanosized $MnWO_4$ was also synthesized by annealing of a precursor obtained by coprecipitation method. The obtained samples were characterized by XRD, SEM, TEM, Raman and IR methods. Raman spectra showed relatively weak dependence on particle size and morphology of the particles. In contrast to this behavior, IR-active bands showed pronounced shifts and changes in relative intensities on particle size and the morphology. Origin of this behavior is discussed.

1. Introduction

$MnWO_4$ has been the subject of extensive studies due to its multiferroic, electrochemical and ionic properties [1–4]. It has also been shown that $MnWO_4$ is a promising material for humidity sensors and high-gain Raman laser [5,6].

It is well known that physical and chemical properties of materials are significantly modified when size of crystallites is of order of nanometers. The properties depend also on morphology of nanoparticles, i.e. they are different for spherical shape particles and one-dimensional (nanotubes, nanowires, nanofibres, nanorods) or two-dimensional (nanoplates) nanostructures [7,8]. Moreover, even for the same morphology, properties may change significantly depending on the growth direction of a nanostructure. For instance, it has been shown that properties of gallium oxide nanowires grown along [0 0 1] direction are different from the nanowires grown along [1 1 0] or [4 0 –1] directions [9]. Changes in optical and catalytic properties have also been reported if nanoscale building blocks form more complex architectures such as flowerlike or tyrelike superstructures [10]. Such organized superstructures have attracted much attention due to their complex functions and potential applications [11,12]. It is, therefore, of great importance to develop synthesis methods, which allow controlling the morphology of the grown nanocrystals, and to study such materials in order to understand the relationship between size and shape of nanoparticles and their properties.

There have been many reports on the synthesis of diverse morphologies of $MnWO_4$ nanoparticles. Nanoplates were synthesized by hydrothermal method and it was shown that they are more suitable for application as humidity sensors than bulk $MnWO_4$ [4]. Solvothermal synthesis was also used to obtain sphericallike particles [13,14], nanorods [13,14], nanofibres [15], nanococcons [16], flowerlike micro-structure composed of nanoplatelets [17], and Urchinlike microspheres assembled by nanorods [18]. Flowerlike particles were also produced using spray pyrolysis [19]. All the reported papers were focused on preparation of nanocrystallites with different size and morphology, and the obtained materials were studied mainly by X-ray powder diffraction (XRD), transmission electron microscopy (TEM) and scanning electron microscopy (SEM). Raman and IR spectra were reported only for flowerlike particles [19] and sphericallike particles or short nanorods [13]. IR spectrum was shown also for Urchinlike microspheres [18]. The IR spectra were presented only above 500 or 400 cm^{-1}. Both IR and Raman spectra were not analyzed in detail in Refs. [18,19]. Some longer discussion was presented only by Tong et al. [13], who attributed the observed shifts of the IR and Raman bands to anisotropic lattice expansion of $MnWO_4$ nanocrystals.

Present paper reports synthesis of nanocrystalline $MnWO_4$ with different size and morphology of the crystallites using hydrothermal and coprecipitation methods. The synthesized materials have been characterized by XRD, TEM, SEM, Raman and IR spectroscopy.

* Corresponding author. Fax: +48 71 3441029.
E-mail address: m.maczka@int.pan.wroc.pl (M. Mączka).

0022-4596/$ - see front matter © 2011 Elsevier Inc. All rights reserved.
doi:10.1016/j.jssc.2011.07.023

The obtained results are compared with those obtained for bulk $MnWO_4$ in order to obtain information how properties of $MnWO_4$ change with morphology and decreasing particle size.

2. Experimental

$MnWO_4$ nanoparticles were synthesized by two different methods using commercial chemicals of analytical grade. In the first, hydrothermal method, 2 mmol of $MnCl_2$ and 25 ml of EA were mixed together and put into an ordinary ultrasonic cleaner until $MnCl_2$ was completely dissolved in EA. Another solution was formed from 2 mmol of $Na_2WO_4 \cdot 2H_2O$ and 1 mmol of CTAB dissolved in deionised water. Both solutions were mixed together under stirring and the suspension formed in this way was poured into the teflon reaction vessel, which was put into a microwave autoclave. Next the introduced preheating at 115 °C was run for half an hour. The hydrothermal reaction was subsequently conducted at isothermal condition for three and half an hour at different temperatures ranging from 150 to 220 °C. After this treatment the reactor was cooled down to room temperature by the water. Resulting powders were filtered off, washed several times with deionised water and finally dried in air at 80 °C for 20 h.

In the second method, 4 mmol of $MnCl_2$ was dissolved in deionised water. Another solution was prepared by dissolving 4 mmol of $Na_2WO_4 \cdot 2H_2O$ in deionised water. Both solutions were mixed together under stirring and the resulting sediment was filtered off, washed several times with deionised water and finally dried in air at 80 °C for 20 h. Thus obtained precursor was annealed for 2 h at different temperatures ranging from 250 to 800 °C.

XRD patterns were recorded at room temperature using X'Pert PRO powder diffractometer (PANalytical, The Netherlands) working in the transmission or reflection geometry, equipped with a linear PIXcel detector and using Cu$K\alpha_1$ radiation ($\lambda = 1.54056$ Å) in the 2Θ range from 5° to 90° with a step of 0.026°.

The particle size and morphology of $MnWO_4$ as well as selected area electron diffraction (SAED) studies were performed using a Philips CM20 SuperTwin transmission electron microscope (TEM) providing 0.24 nm resolution and a FEI Nova NanoSEM 230 microscope. Acquisition and interpretation of EBDS (Electron Back Scattered Diffraction) patterns were done with EDAX OIM XM 4 system attached to FEI Nova NanoSEM 230 microscope. Composition of the samples was checked with energy dispersive spectroscopy (EDS) standard-less analysis. EDS spectra were acquired and analyzed using EDAX OIM XM 4 system attached to FEI Nova NanoSEM 230 microscope. Powders for SEM and EDS analyses were dispersed on high purity carbon stubs. Specimens for TEM were prepared by grinding the samples in mortar and dispersing in methanol with ultrasonic agitation. A droplet of suspension was deposited on a microscope grid covered with carbon film.

Infrared spectra were measured with a Biorad 575C FT-IR spectrometer both in KBr pellet and nujol suspension for the 4000–400 cm^{-1} region and in nujol suspension for the 500–50 cm^{-1} region. Raman spectra were measured using Bruker FT 100/S spectrometer with the YAG:Nd laser excitation (1064 nm). Both IR and Raman spectra were recorded with a spectral resolution of 2 cm^{-1}.

3. Results and discussion

3.1. X-ray powder diffraction

Figs. 1 and 2 show representative XRD patterns of the samples prepared by hydrothermal method at 150, 160, 170, 180, 190, 200 and 220 °C (samples H-150, H-160, etc.) and coprecipitation

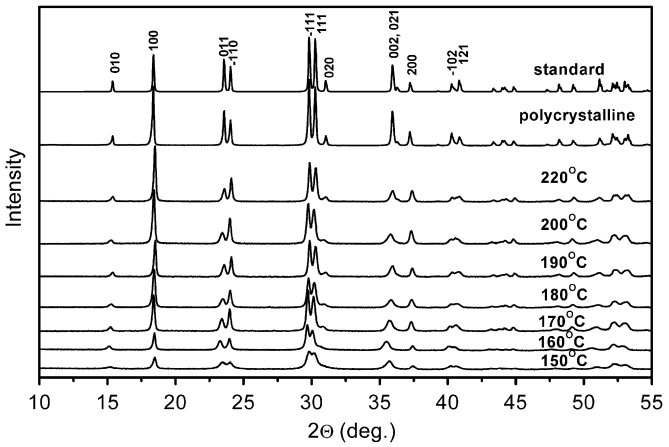

Fig. 1. XRD patterns of the polycrystalline (bulk) and nanocrystalline $MnWO_4$ samples prepared by hydrothermal method. The standard pattern of $MnWO_4$ generated by powder diffraction diagram simulation program Poudrix V2 [20] using the published single crystal data [21] is presented at the top.

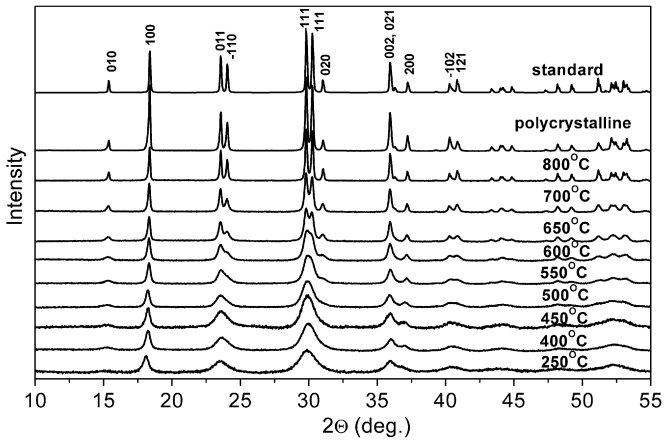

Fig. 2. XRD patterns of the nanocrystalline $MnWO_4$ samples prepared by coprecipitation method. The standard pattern of $MnWO_4$ calculated on the basis of single crystal data is presented at the top.

method followed by annealing at 250, 400, 450, 500, 550, 600, 650, 700 and 800 °C (samples C-250, C-400, C-450, etc.), respectively. For the comparison sake, the XRD pattern of the powdered single crystal of $MnWO_4$ (named as polycrystalline sample) and the calculated standard pattern of $MnWO_4$ are also presented.

The XRD patterns of the synthesized samples could be indexed to monoclinic wolframite-type phase of $MnWO_4$ [21] (see Figs. 1 and 2). Significant broadening of all diffraction peaks clearly shows that the nanocrystalline phases of $MnWO_4$ are formed. Figs. 1 and 2 show that the peaks become sharper with increase of the synthesis temperature that implies that the particle size increases. The average size of coherently diffracting nanocrystals perpendicular to the diffraction ($h\,k\,l$) plane was calculated from the full width at half maximum (FWHM) of the diffraction peak under the Scherrer approximation: $D = K\lambda/\beta \cos\Theta$, where D is the mean crystal size along the [$h\,k\,l$] direction, λ is the X-ray wavelength (in our study $\lambda = 1.54056$ Å), β is the FWHM of the diffraction line (in radians), Θ is the angle of diffraction, and the Scherrer constant K is conventionally set to 1.0 [22–25]. The contribution from instrumental broadening was removed by subtracting the FWHM of the corresponding line of well-annealed, bulk crystal. Since the actual profiles are neither purely Gauss nor purely Cauchy (Lorentz), we have used the Halder–Wagner parabolic approximate relation for the true diffraction profile: $\beta = \sqrt{B^2 - b^2}$, where B and b are the measured

FWHM of the equivalent diffraction lines in the specimen and the reference sample, respectively [24–28]. In our case the data from the powdered single crystal (bulk sample) is used as a reference.

Average particle size along 100, 010, −110 and 011 directions as a function of the synthesis temperature is presented in Fig. 3. Fig. 3a indicates that particles in the samples synthesized by the surfactant-assisted hydrothermal method have much larger dimension along the *a* axis than along the *b* axis. Increase of the synthesis temperature leads to increase of the average particle size but this increase is quite irregular (see Fig. 3a). It is worth pointing that for the H-220 sample the ratio of intensity between the (0 1 0) and (1 0 0) peaks is much lower than the standard value (0.119 versus 0.285). The ratio between (0 1 1) and (1 0 0) peaks is also much lower than the standard value (0.312 versus 0.919). These data indicate that the (1 0 0) facets of the prepared $MnWO_4$ nanocrystallites are preferentially oriented parallel to the supporting surface. When synthesis temperature decreases, the ratios increase indicating that the preferential orientation of the crystallites becomes less pronounced. It becomes negligible for the H-150 and H-160 samples. Our results also show that the lattice parameter *b* of the H-190 and H-220 samples is slightly lower than that observed for the polycrystalline sample and this parameter increases with decreasing synthesis temperature by about 0.8% and 1.4% for the H-150 and H-160 sample, respectively (see Fig. 4b). Similar behavior is observed for the lattice parameter *c*, which increases by about 0.5% and 1% for the H-150 and H-160 sample, respectively (Fig. 4c). Different behavior is observed for the parameter *a*. This parameter is smaller when compared to the polycrystalline sample for all nanocrystalline samples and the largest decrease of about 0.8% is observed for the H-190 sample (see Fig. 4a). Fig. 4d shows also that the difference δ between the value of the *c* and *a* parameters changes very slightly in the 170–220 °C range but increases significantly for the H-150 and H-160 samples. Splitting Δ between (1 1 1) and (−1 1 1) peaks decreases slightly in the 170–220 °C range and more significantly for the H-150 and H-160 samples (see Fig. 4f). The observed decrease of Δ indicates decrease of the monoclinic angle, i.e. it implies slight decrease of the monoclinic distortion with decreasing particle size. It is worth noting that observation of some structural changes with decreasing particle size is very often reported for nanocrystalline materials. As emphasized by Ayyub et al. [29] the lattice almost invariable becomes more symmetric as the size is decreased. The structure of $MnWO_4$ is monoclinic but it has been shown that it may be considered as a slightly distorted orthorhombic one described by the space group *Pmcm* (D_{2h}^5) [30,31]. It is, therefore, likely that with decreasing particle size symmetry of the crystallites becomes closer to the *Pmcm* one.

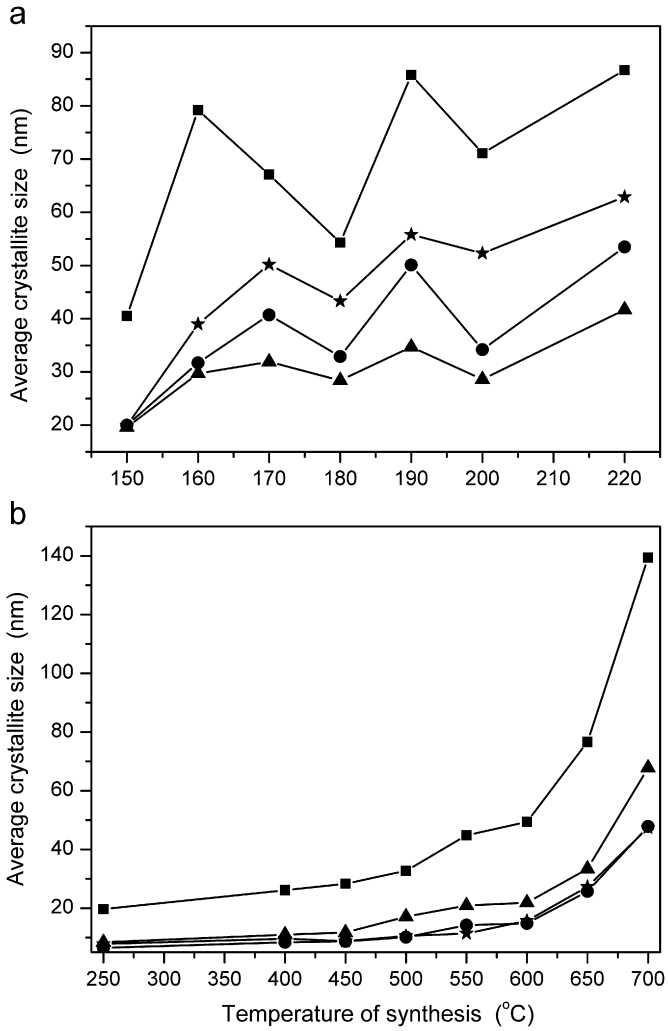

Fig. 3. Average crystallite size along 100 (squares), −110 (stars), 010 (circles) and 011 direction (up triangle) as a function of the synthesis temperature for the samples prepared by (a) hydrothermal method and (b) coprecipitation method. Solid lines are guide for the eye.

Fig. 3b indicates that the particles in the C-250 sample also have much larger dimension along the *a* axis (about 20 nm) than along the *b* axis (about 6 nm). The size of the particles increases in a regular way with increase of the synthesis temperature. For the sample prepared at 800 °C the broadening of diffraction lines is small indicating large size of the particles. It is also worth pointing that the samples synthesized by the coprecipitation method do not show any clear preferential orientation of the crystallites. The parameters *a* and *b* of the C-800 sample are in good agreement with those observed for the polycrystalline sample and they increase with decreasing synthesis temperature by about 1.4% and 1.3%, respectively, for the C-250 (see Fig. 4g and h). In contrast to this behavior, the parameter *c* exhibits very weak changes, i.e. the largest decrease of about 0.4% is observed for the C-400 sample (Fig. 4i). Fig. 4k and l shows also that both δ and Δ parameters decrease significantly with decreasing particle size.

3.2. SEM studies

SEM of the H-150 sample shows that it consists of rods or ribbons assembled into a bunch, and then these bunches are assembled forming larger structures (Fig. 5a). The length of these rods or ribbons is about 200–600 nm and their width or thickness is below 100 nm. EDS analysis confirms that these particles have composition close to $MnWO_4$. Although SEM images show that the rods are relatively large, our XRD pattern indicates large broadening of the diffraction peaks. This result shows that the rods or ribbons are composed of smaller crystallites. The H-160 sample has a significantly different morphology, i.e. it consists of barlike particles up to 1.2 μm long and 0.6 μm wide (Fig. 5b). Fig. 5b clearly shows that these particles are not single crystals but are assembled by much smaller particles. Interestingly, some of these barlike particles are assembled in larger microcrystals, which look like a very imperfect flower as a whole (see top-left corner of Fig. 5b). When synthesis temperature increases to 170 °C, the as-prepared product is composed mainly of hierarchical platelike spherical microcrystals with a diameter up to 3 μm (Fig. 5c). Each of these flowerlike microcrystals is composed of petals and these petals are assembled by smaller particles. The H-180 sample is less homogenous. It also contains flowerlike microcrystals with diameters up to 3 μm but petals of these microcrystals are much narrower than those observed in the H-170 sample (Fig. 5d). Moreover, this sample contains large amount of barlike particles, which are poorly assembled. The

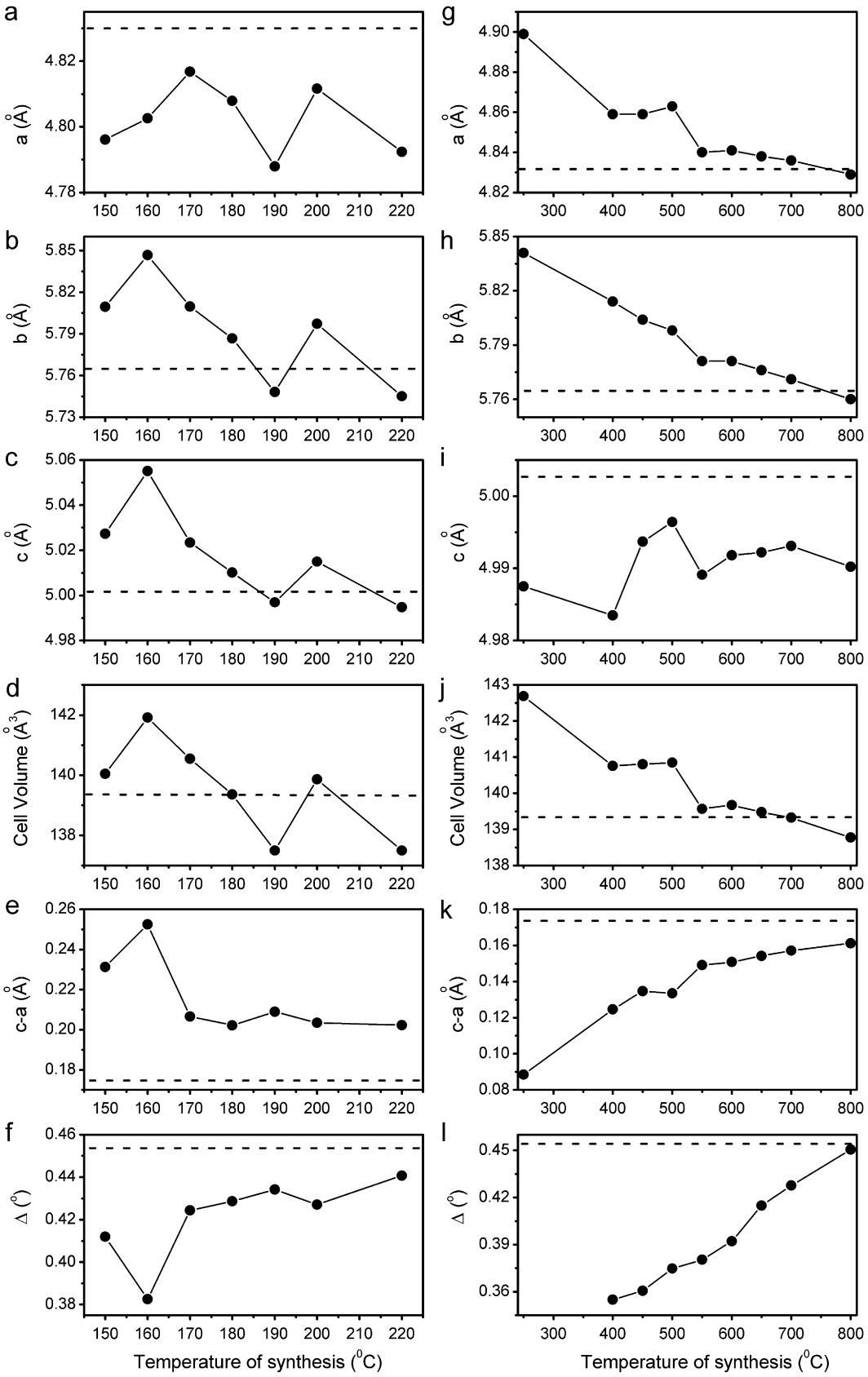

Fig. 4. Lattice parameters, unit cell volume, the difference between the parameters *c* and *a* as well as splitting between (1 1 1) and (−1 1 1) diffraction peaks (Δ) for the H-samples (panels a–f) and C-samples (panels g–l).

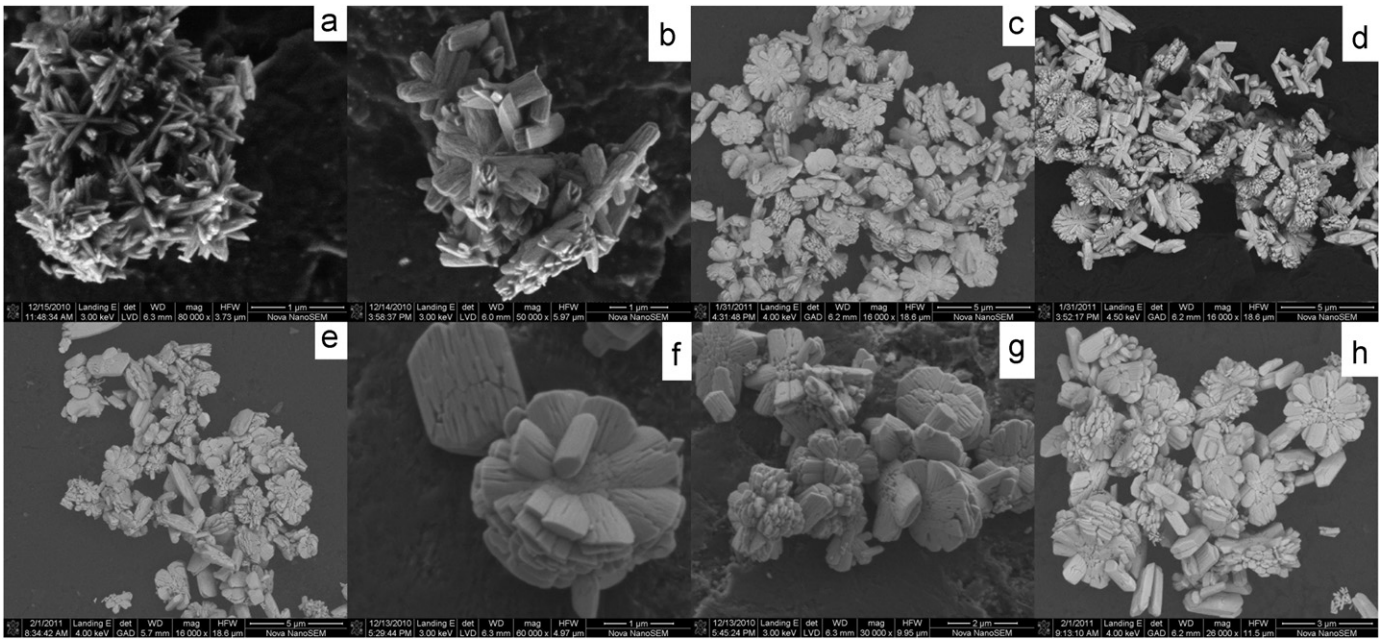

Fig. 5. SEM images of $MnWO_4$ particles prepared by hydrothermal process at: (a) 150 °C, (b) 160 °C, (c) 170 °C, (d) 180 °C, (e) 190 °C, (f,g) 200 °C, and (h) 220 °C.

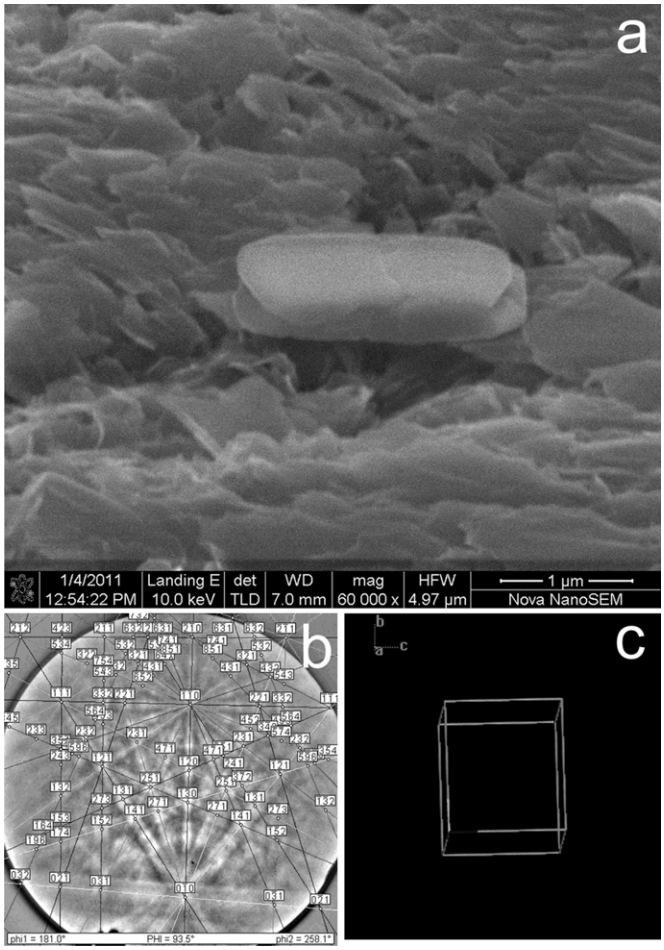

Fig. 6. SEM image of large barlike particle of H-220 sample given with corresponding indexed EBSD pattern. An orientation of the unit cell relative to sample holder (stub) normal is also given. The measured pattern could be indexed in $MnWO_4$ monoclinic structure (PDF—0,800,135).

H-190 sample is similar to the H-180 sample but the barlike particles are larger and petals of the flowerlike microcrystals are broader (Fig. 5e). It is worth noting that smaller size of petals for the H-180 sample, when compared to the H-170 and H-190 samples, is consistent with the X-ray diffraction results, i.e. with the minima observed at 180 °C in the plot of crystallite size as a function of the synthesis temperature presented in Fig. 3. When synthesis temperature increases to 200 °C, morphology and size of the synthesized particles do not show large changes (see Fig. 5f and g). However further increase in width and thickness of the barlike particles and petals occurs at 220 °C (Fig. 5h). In order to obtain some additional information, EBSD patterns were recorded for a few barlike particles prepared at 220 °C. A representative result is presented in Fig. 6. EBDS analysis indicates that the *c* axis is parallel to the bar axis. The particles often lay flat on the support with *a* axis normal to the surface. These conclusions are in agreement with XRD pattern, where a texture is clearly seen, i.e. (*h* 0 0) reflections are enhanced (see Fig. 1).

SEM of the C-400 sample shows that it is composed of platelike nanoparticles assembled to form flowerlike clusters (Fig. 7a). The thickness of these plates is ca. 15–20 nm. When synthesis temperature increases, the morphology of the particles is preserved (see Fig. 7b–d). However, their lateral size and thickness increase. For instance, the thickness of the particles increases to ca.20–30 nm for the C-550 and C-650 samples, and 30–60 nm for the C-800 sample.

3.3. TEM studies

Fig. 8a–d shows typical individual nanoparticles for the H-150 (Fig. 8a), H-160 (Fig. 8b), H-200 (Fig. 8c) and H-220 samples (Fig. 8d), which assembly into hierarchical $MnWO_4$ architectures. The length (width) of these particles increases with increasing temperature from ca. 30–100 (10–35) nm for the H-150 sample to ca. 150–600 (60–160) nm for the H-220 sample. The high resolution TEM (HRTEM) images recorded on individual $MnWO_4$ nanoparticles in the H-150 sample show clear lattice fringes (Fig. 8e). This observation indicates the highly crystalline nature

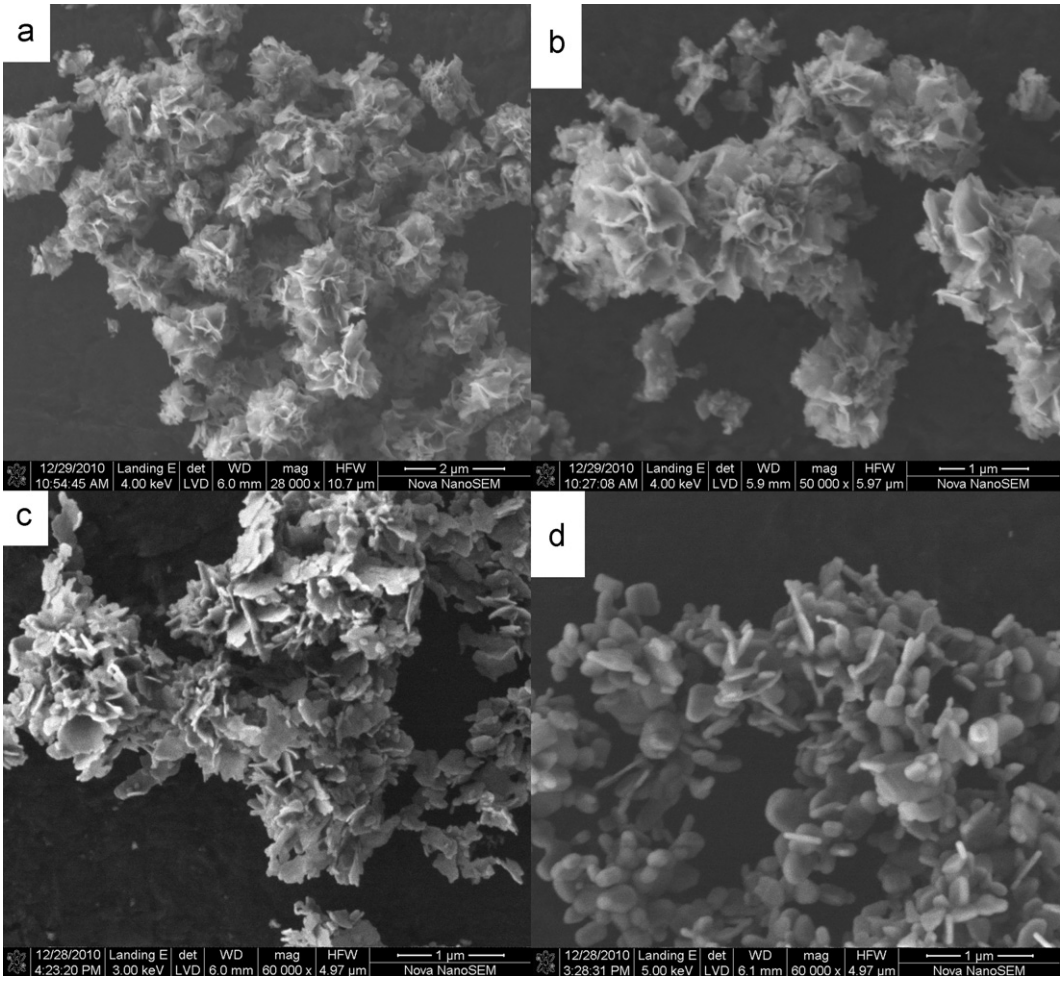

Fig. 7. SEM images of $MnWO_4$ particles prepared by coprecipitation process and annealing at: (a) 400 °C, (b) 550 °C, (c) 650 °C and (d) 800 °C.

of these nanoparticles. The lattice fringe spacing is 5.8 Å (Fig. 8e, left side) and 3.8 Å (Fig. 8e right side). These spacings correspond well to the separation between (0 1 0) and (0 1 1) planes of $MnWO_4$, respectively. HRTEM and the pattern from selected area electron diffraction (SAED) of single particle in the H-220 sample confirm that it is a single crystal of $MnWO_4$ and shows that the crystal growth is in the *c* direction (Fig. 8f).

TEM image and SAED pattern of the C-400 sample presented in Fig. 9a shows that the sample is composed of strongly aggregated nanosized crystals with different orientations. HRTEM image confirms that larger particles consist of the highly crystalline nanocrystals (Fig. 9b). The lattice fringe spacing observed in Fig. 9b corresponds well to the separation between (0 1 0) and (0 1 1) planes. This image indicates that the dimension of the observed crystallites is about 20–25 nm along the *c* axis and about 6 nm along the *b* axis.

3.4. Formation mechanism

On the basis of the above experimental observation, we may speculate the formation mechanism of the hierarchical $MnWO_4$ architectures. First of all it is worth noting that according to the literature data MWO_4 wolframites (M=Mn, Co, Fe, Zn) have tendency to grow in shape of nanorods or nanoplates under hydrothermal conditions [13,14,17,32,33]. When a surfactant is added to the reaction mixture, the growth habit is not changed but the crystallites may assembly into Urchinlike microstructures, as observed for CTAB-assisted hydrothermal growth of $MnWO_4$ [18]. It is, therefore, obvious that EA played a very important role in formation of the observed, by us, self-assembled architectures. Literature data show that at low temperatures some organic compounds, such as diaminoalkanes or phenylenediamine, can be intercalated into $MnWO_4$ structure leading to formation of stable complexes [34,35]. The molecules are intercalated between the (0 1 0) planes and this example shows that some molecules may adhere to the (0 1 0) plane of $MnWO_4$ reducing the growth rate in [0 1 0] direction. The small size of $MnWO_4$ nanocrystals along the [0 1 0] direction, as evidenced from XRD patterns, is consistent with strong adhesion of EA molecules to the (0 1 0) plane. We suppose, therefore, that at an early stage of crystallization, nanoplates are formed by stabilization of (0 1 0) crystal surface by EA. These nanoplates aggregate parallel each to other by self-assembly process forming long rods and ribbons in the [0 0 1] direction. Then these rods and ribbons self-assemble into larger radial structures due to presence of CTAB surfactant molecules. With longer time of the synthesis, more nanoplates attach this radial structure and the rods and ribbons become longer and thicker. When synthesis temperature increases, the nanoplates grow in a faster way and they self-assemble forming larger petals of the flowerlike microcrystals.

3.5. Raman and IR spectra of $MnWO_4$—selection rules and assignment of modes

The monoclinic C_{2h}^4 unit cell of the studied crystal comprises 12 atoms, which have 36 zone-center degrees of freedom described by

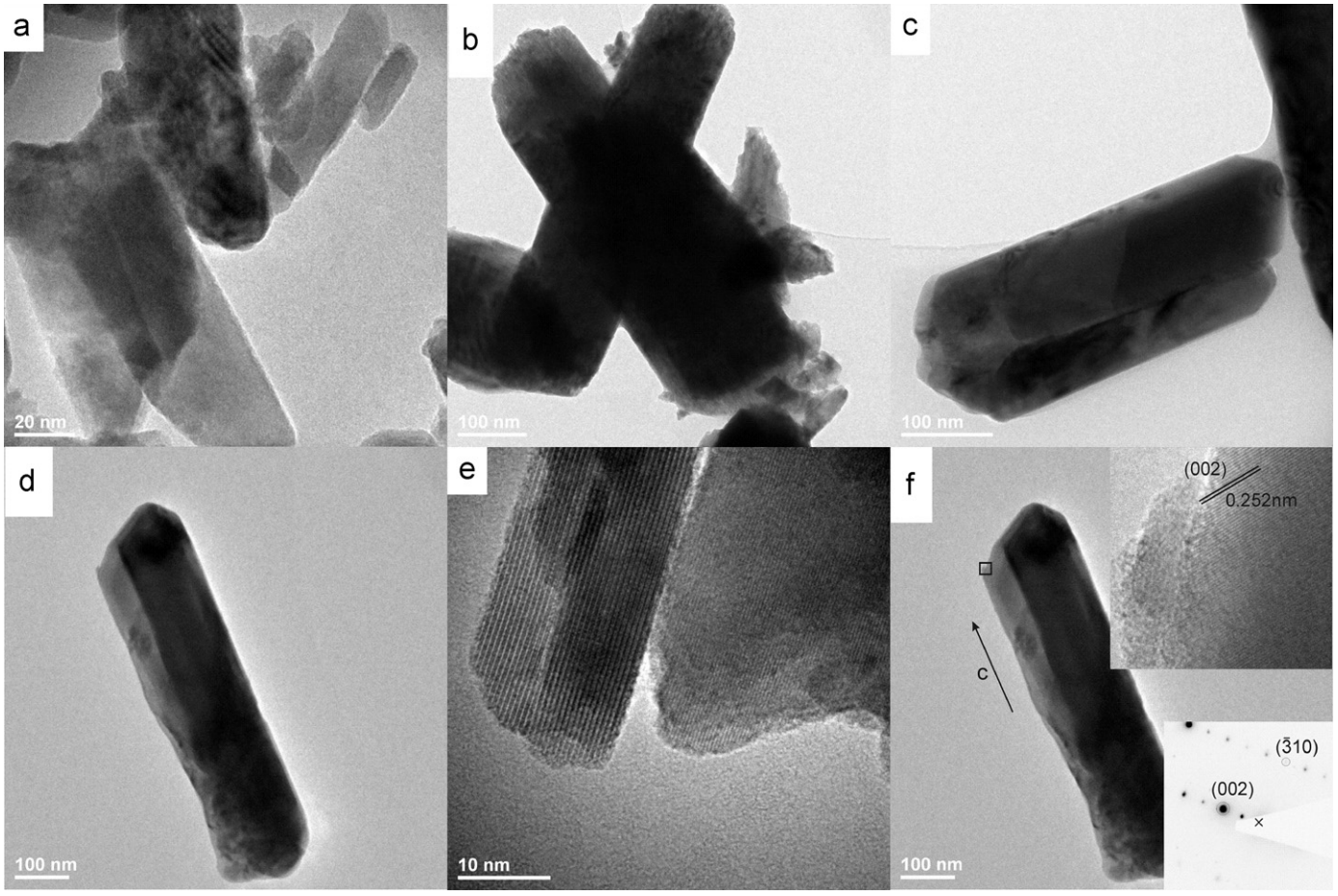

Fig. 8. TEM images of individual $MnWO_4$ particles prepared by hydrothermal process at (a) 150 °C, (b) 160 °C, (c) 200 °C, and (d) 220 °C. (e) HRTEM image taken on two typical particles prepared at 150 °C. The lattice fringe spacing is 5.8 and 3.8 Å for the particle seen on the left and right side, respectively. (f) HRTEM image and SAED pattern of the individual $MnWO_4$ particle prepared at 220 °C.

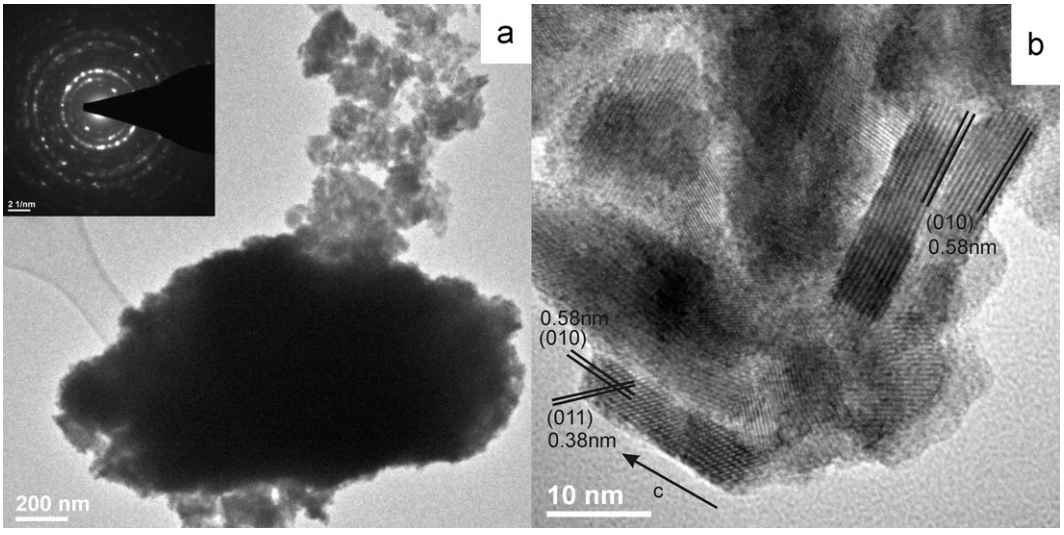

Fig. 9. (a) TEM image of $MnWO_4$ particles prepared by coprecipitation process and annealing at 400 °C. The inset shows the SAED pattern. (b) HRTEM image taken on typical particle prepared at 400 °C.

irreducible representation of the factor group C_{2h} as $8A_g+8A_u+10B_g+10B_u$. Three of these modes, A_u+2B_u, are acoustic modes. The optic modes can be subdivided into $2A_g+A_u+4B_g+2B_u$ translational modes of the Mn and W atoms and $6A_g+6A_u+6B_g+6B_u$ modes involving oxygen atoms. Among these modes the A_g and B_g modes are Raman-active whereas the A_u and B_u modes are IR-active. This analysis shows that one expects to observe 15 and 18 modes in IR and Raman spectra of $MnWO_4$, respectively.

Raman and IR spectra of the obtained nanocrystalline powders as well as bulk $MnWO_4$ are presented in Figs. 10 and 11, 13–15. Detailed assignment of IR and Raman bands on the basis of lattice dynamics calculations and polarized IR studies was presented in detail in our recent paper [36], and will be not discussed in the present paper. Here we recall only a few most important conclusions. First, the Raman-active A_g modes are observed at 884, 698, 545, 398, 326, 258, 206 and 129 cm^{-1} whereas the B_g modes at 774, 674, 511, 357, 294, 272, 178, 166, 160 and 90 cm^{-1}. Second, the transverse optical (TO) and longitudinal optical (LO) IR-active modes of A_u symmetry are as follows: 861 (897), 656 (753), 495 (536), 420 (428), 348 (373), 307 (308) and 182 (192) cm^{-1} (the LO values are given in parentheses). The corresponding IR-active modes of B_u symmetry are observed at 795 (901), 577 (739), 458 (472), 324 (382), 280(281), 248 (273), 209 (220) and 147 (153) cm^{-1}. Third, the Raman and IR bands in the 770–890 cm^{-1} range can be assigned to symmetric and asymmetric stretching modes of the short W–O2 bonds. Fourth, the bands in the 600–700 cm^{-1} range can be assigned to stretching modes of the double oxygen bridge involving W–O1 bonds. Fifths, translational motions of W and Mn atoms contribute strongly to the modes observed below 290 cm^{-1} and the remaining modes in the 550–290 cm^{-1} range can be assigned to the WO_6 bending modes [36].

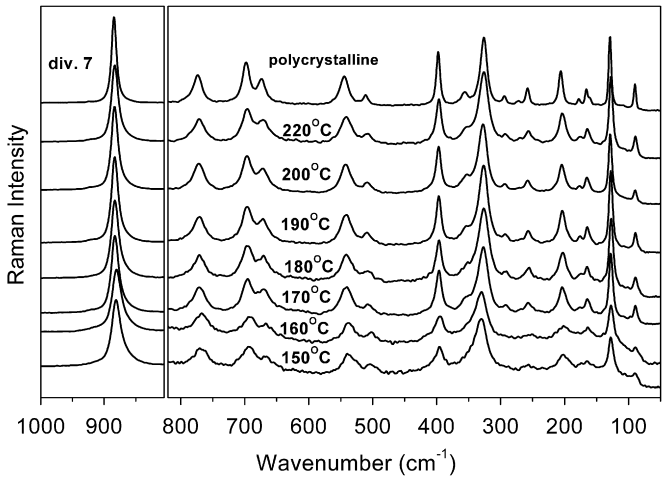

Fig. 10. Raman spectra of the polycrystalline (bulk) and nanocrystalline $MnWO_4$ samples prepared by the surfactant-assisted hydrothermal method.

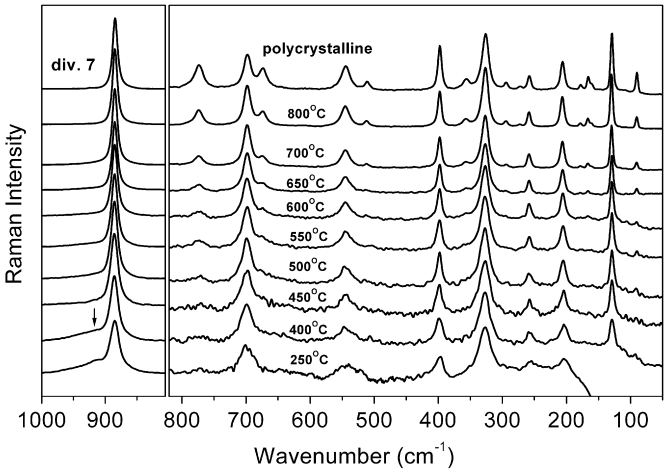

Fig. 11. Raman spectra of the nanocrystalline $MnWO_4$ samples prepared by coprecipitation method. Arrows indicate additional broad band at ca. 920 cm^{-1}, which originate from defects.

3.6. Raman spectra of the $MnWO_4$ nanocrystalline samples

Figs. 10–12a show that the Raman spectra of $MnWO_4$ synthesized by hydrothermal and coprecipitation methods exhibit some changes with decreasing crystallite size. First, width of the observed bands increases. For instance, the bandwidth of the most intense Raman band at 884 cm^{-1} is 9.3, 18.1 and 16.3 cm^{-1} for the polycrystalline, H-150 and C-250 sample, respectively. Second, a number of bands exhibit wave number decrease or increase. These changes are very weak for the samples prepared by coprecipitation method. The largest downshift (about 2 cm^{-1}) is observed for the 206 cm^{-1} band of the C-250 sample. Much larger shifts are observed for the samples synthesized by the hydrothermal method (see Fig. 12a). For instance, for the H-150 sample the most pronounced downshift is observed for the 884 (3.9), 774 (5.1), 698 (4.3), 674 (8.3), 545 (7.4), 511 (9.8), 357 (10.6) and 206 cm^{-1} (4.6 cm^{-1}) bands (shifts are given in parentheses). Upshift (about 3.5 cm^{-1}) is observed only for the 326 cm^{-1} Raman band. Third, a number of bands for the samples synthesized by coprecipitation method exhibit intensity decrease with decreasing particle size. This behavior is especially pronounced for the 774, 674, 511, 357 and 294 cm^{-1} bands, which correspond to the modes of B_g symmetry [36]. Fourth, a clear band becomes visible at ca. 920 cm^{-1} for the C-400 and C-250 samples.

The question that arises is what are the reasons of the observed changes. First of all, the band at ca. 920 cm^{-1} for the C-400 and C-250 samples can be assigned to surface defects, as proposed recently for $MnWO_4$ nanocrystals obtained by simple hydrothermal method [13]. Regarding the observed shifts and broadening of bands, it is well known that for a nanocrystalline material such changes in phonon properties can be attributed to creation of defects, distribution of crystallite size, changes of the lattice parameters (strain), phonon confinement effect and variation in phonon relaxation time [37–39]. Moreover, as a result of the phonon confinement the bands become asymmetric. The observed broadening of Raman bands for our $MnWO_4$ samples and clearly asymmetric shape of the strongest Raman band for the H-samples can be understood in terms of phonon confinement effect and creation of defects in the nanosized samples. The phonon confinement effect may lead to both negative and positive shifts of a Raman band, depending on shape of the phonon dispersion curves [37–39]. Although there are no reports on phonon dispersion for $MnWO_4$, such data are available for isostructural $CdWO_4$ [40]. These data show that nearly all Raman active modes exhibit weak dispersion near the Brillouin zone center and therefore weak and negative shift of Raman bands with decreasing particle size is expected for majority of modes. It is worth noting, however, that positive shift is expected for the 310 cm^{-1} Raman band of $CdWO_4$ [40], which corresponds to the 326 cm^{-1} band of $MnWO_4$. Our data show weak and negative shifts for majority of modes when synthesis temperature decreases from 220 to 170 °C. However, more significant and negative changes are observed when temperature decreases further to 160 to 150 °C. The only exception is the 326 cm^{-1} band, which exhibits positive shift, in agreement with prediction based on phonon confinement effect. This result indicates that the observed shifts can be attributed, at least partially, to phonon confinement effect. It is worth noting, however, that the H-160 sample exhibits larger shifts than the H-150 sample, in spite of larger crystallite size in the former case. As presented in Fig. 4, the parameters b and c show much more pronounced increase for the H-160 sample than for the H-150 sample. We may, therefore, conclude that second contribution to the observed shifts comes from changes in the lattice parameters (strain), which in turn lead to changes in the bond lengths and angles. This contribution can

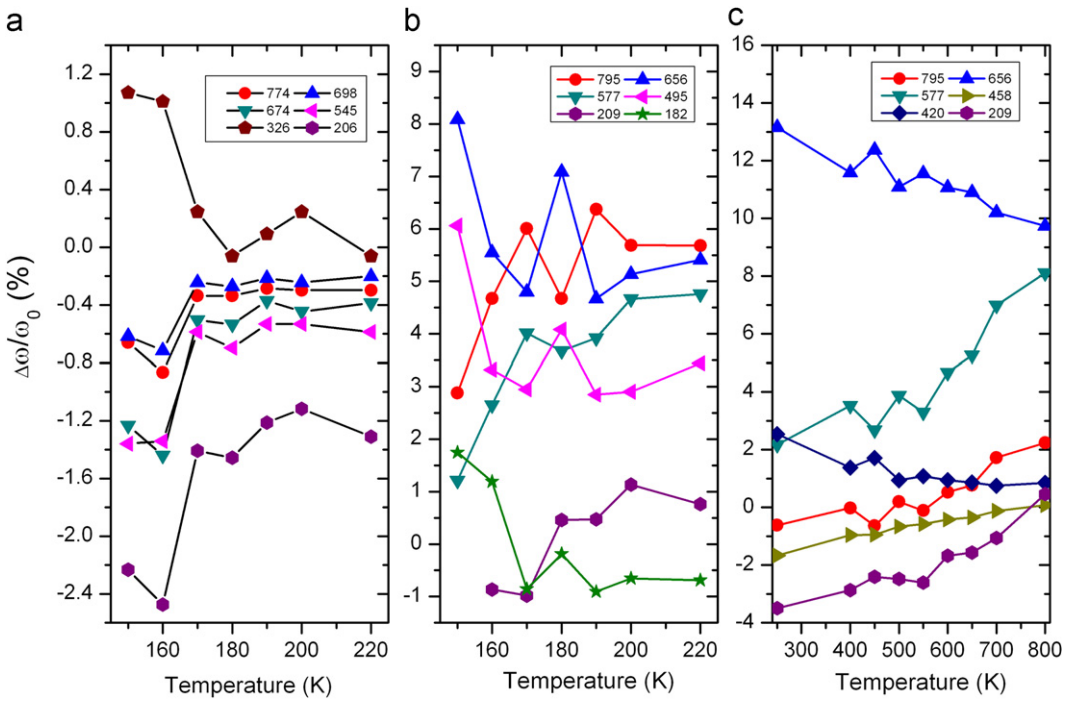

Fig. 12. (a) Relative shifts of given Raman modes as a function of synthesis temperature for the samples synthesized by the hydrothermal method. ω_0 denotes wave number for the bulk $MnWO_4$. (b) relative shifts of given IR modes as a function of synthesis temperature for the samples synthesized by the hydrothermal method and (c) by coprecipitation method. For IR modes ω_0 denotes TO wave number for bulk $MnWO_4$.

be estimated from the following equation [37]:

$$\Delta w = -\gamma \omega_0 \Delta V / V_0 \quad (1)$$

where $\Delta\omega$ is Raman shift, ω_0 is Raman wave number of bulk, γ is the Grüneisen parameter, ΔV is the change in unit cell volume and V_0 is the unit cell volume of bulk. The Grüneisen parameters for $MnWO_4$ are not known but they are known for isostructural $ZnWO_4$ [41]. All of them are positive. As shown in Fig. 4d, the unit cell volume of the H-220 sample is lower than for bulk and increases with decreasing particle size. Therefore, for the H-220 sample the strain contribution should be positive and should change to negative for H-170, H-160 and H-150 samples (see Fig. 4d).

Behavior of the samples prepared by the coprecipitation method is more difficult to understand. Since the samples synthesized below 600 °C have smaller crystallite size than the H-150 and H-160 samples, they should exhibit more significant negative shifts due to phonon confinement effect than the H-150 and H-160 samples. Moreover, the unit cell volume for the C-samples increases with decreasing particle size and the increase for the C-250 sample is larger than for the H-160 sample (see Fig. 4d and j). Therefore, shift of Raman bands due to strain should also be negative and larger for the C-250 sample than for the for the H-160 sample. Surprisingly, Raman bands exhibit nearly no shifts. We suppose that the negative shifts due to phonon confinement effect and increase of the unit cell volume are compensated by another positive contribution of an opposite sign. Here it is important to emphasize that the Eq. (1) is valid for cubic crystals, which exhibit isotropic compression and thermal expansion. However, monoclinic $MnWO_4$ is strongly anisotropic and, therefore, wave number of a particular mode may exhibit different shift if the same change of the lattice parameter *a, b* or *c* occurs. Moreover, changes in the monoclinic distortion may also affect wave number of a mode. Comparison of the X-ray diffraction results shows that the H- and C-samples exhibit quite different dependence of the lattice parameters *a* and *c*, i.e. whereas for the H-samples the difference $\delta = c - a$ is higher than for bulk and increases with decreasing particle size, the opposite behavior is observed for the C-samples. The splitting Δ, which reflect the change in the monoclinic distortion, decreases both for the H-and C-samples, being larger for the C-samples (see Fig. 4f and l). We suppose, therefore, that the positive contribution to the Raman shifts for the C-samples might be related to decrease of the δ parameter with the decreasing particle size, which results in some specific changes in the bond lengths and angles leading to slightly positive shifts of the Raman modes. Defects produced in these samples may also contribute to this behavior, since these samples were prepared by annealing of precipitate, which according to the literature data is manganese tungsten hydrate with water molecules intercalated between the (0 1 0) planes of $MnWO_4$ [34,35]. Such synthesis may lead to defects and some local inhomogeneity.

The intensity decrease with decreasing particle size for the B_g symmetry modes observed by us is difficult to understand. It is clear that this behavior cannot be explained by preferential orientation of $MnWO_4$ crystallites, since the X-ray diffractograms do not show any preferential orientation and the measured Raman spectra were always the same, irrespective of the scattering configuration and preparation of the samples for the measurements. Decrease of the monoclinic distortion as a cause of this peculiar behavior can also be excluded, since the H-160 sample does not show this behavior, in spite of significant decrease of the monoclinic distortion. We suppose, therefore, that this puzzling behavior may be due to presence of defects and some local structural changes in the C-samples. It is interesting to notice that similar change in intensity of the B_g Raman bands was recently also observed for $MnWO_4$ nanoparticles prepared using spray pyrolysis but origin of this behavior was not discussed [19].

3.7. *IR spectra of the $MnWO_4$ nanocrystalline samples*

IR bands show much more pronounced shifts with decreasing particle size and change of particle morphology than the Raman

bands (see Figs. 12b, c, 13–15). This behavior can be well observed in Fig. 12b and c, which show wave number dependence of some IR modes on the synthesis temperature. As can be seen in these figures, position of some bands may vary in a very broad wave number range. For instance, the 818 cm^{-1} for the polycrystalline sample shifts to 846 cm^{-1} for the H-190 sample and 790 cm^{-1} for the C-250 sample. Similarly as discussed above for the Raman-active modes, phonon confinement effect is expected to lead to weak shifts also for the IR-active modes. It is, therefore, unlikely that this effect is significant enough to cause such large IR bands' shifts. Such large shifts cannot also be attributed to strain, defects or some structural changes since in such case pronounced changes should also be observed in the Raman spectra. Inspection of the previous results obtained for $MnWO_4$ single crystal indicates that change in an IR band position is correlated with magnitude of the splitting between TO and LO modes, i.e. the larger the splitting, the more pronounced changes in bands' position are observed. This fact proves that the observed effect can be attributed mainly to the effect of long-range polarization. Indeed, literature data show that shape and maximum intensity of an IR absorption band can be very dependent upon the size and shape of the specimen due to the long-range Coulomb forces [39,42–44]. For instance, in ionic crystals the surface modes may appear and IR bands may shift to higher wave numbers due to increased polarization charge at the surface of the nanoparticles [39,45]. As a result, the maximum absorption of an IR band may be located between TO and LO. This effect is observed already for the polycrystalline sample (see Figs. 13–15).

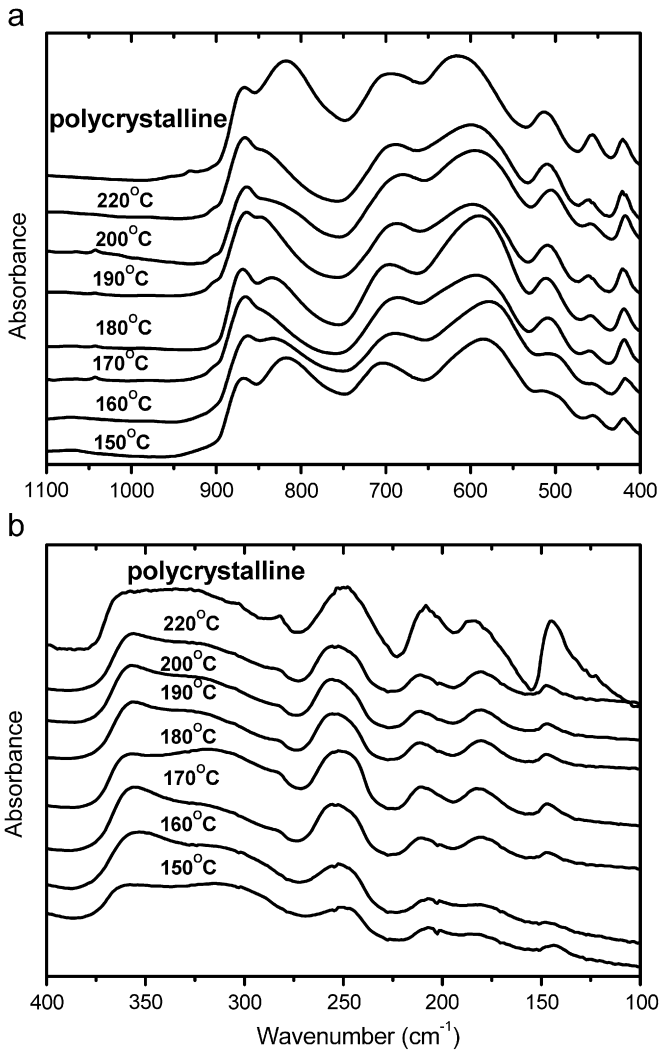

Fig. 13. (a) Mid-IR (in nujol) and (b) far-IR spectra of the polycrystalline (bulk) and nanocrystalline $MnWO_4$ samples prepared by the hydrothermal method.

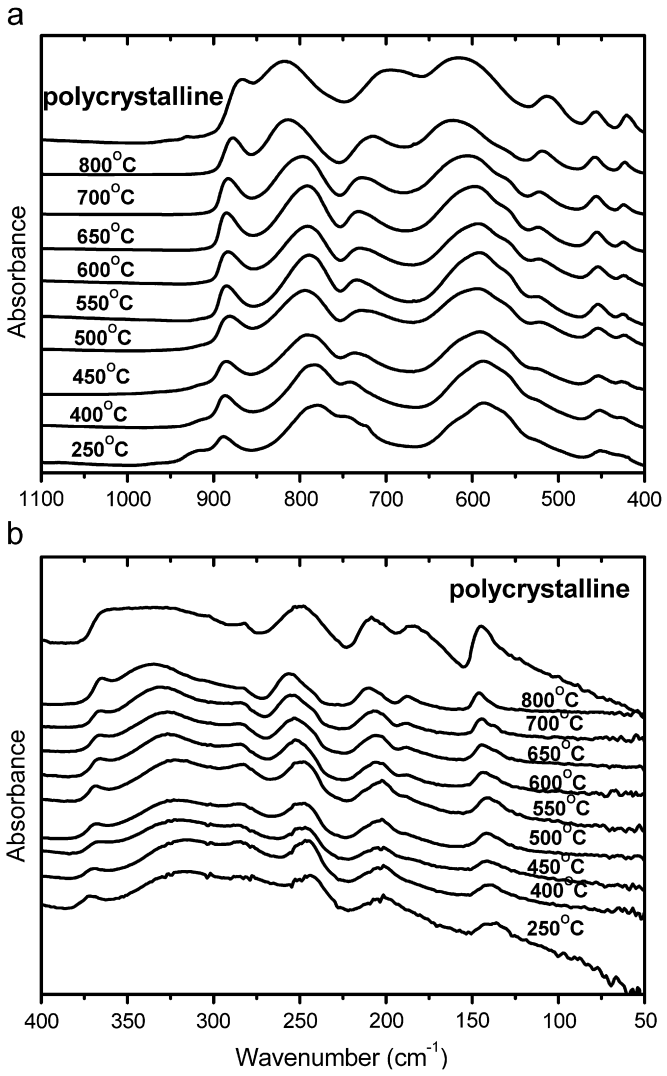

Fig. 14. (a) Mid-IR (in nujol) and (b) far-IR spectra of the nanocrystalline $MnWO_4$ samples prepared by coprecipitation method.

It has been shown that for cubic crystals maximum absorption can be calculated from the known LO–TO splitting for different shapes of nanocrystals [44]. For instance, a thin platelike crystal will absorb near LO mode for polarization perpendicular to the large surface and near TO for polarization parallel to this surface [44]. On the other side, long rodlike particle will absorb near TO for polarization parallel to the rod axis and between TO and LO for polarization perpendicular to the rod axis [44]. This behavior was shown for cubic crystals and it is expected to be more complicated for low symmetry crystals, like studied here monoclinic $MnWO_4$. It is also worth pointing that the maximum absorption of a surface mode shifts to lower wave numbers with increase of the dielectric constant of the surrounding medium [44,46]. On the other hand, if particle aggregations are formed, the dipole–dipole interactions between particles may give rise to broadening and shift of surface modes band [46].

Let us now discuss the observed changes in the IR spectra in more details. Figs. 13–15 show that when surrounding medium changes form nujol to KBr, the IR bands become significantly narrower. Moreover, the bands exhibit slight shifts. These shifts are both positive and negative. Therefore, they cannot be attributed

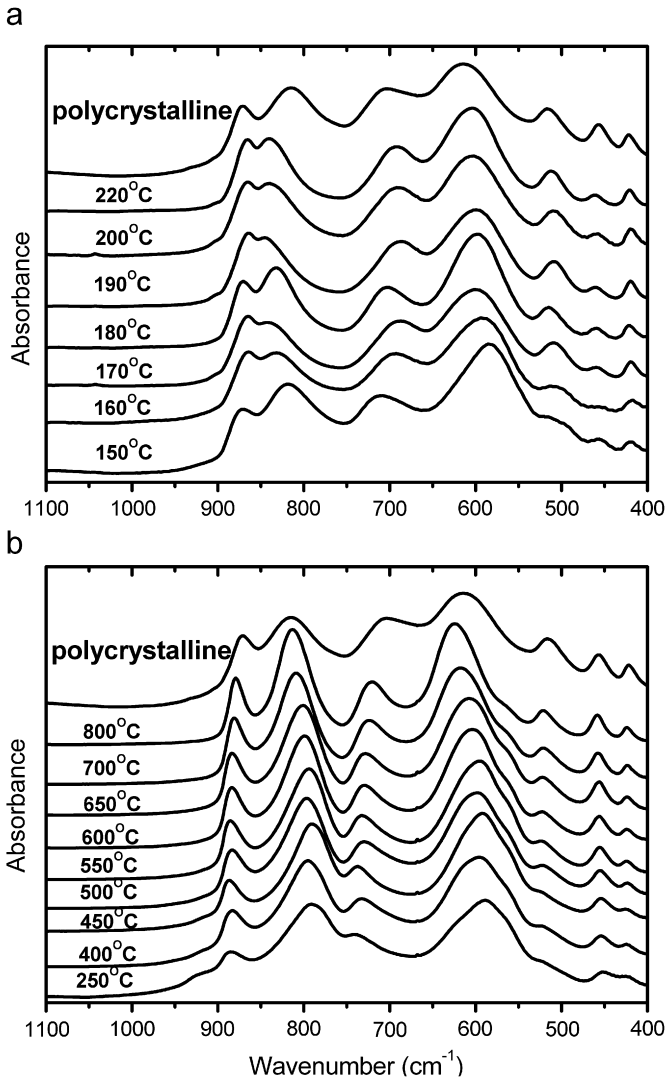

Fig. 15. (a) Mid-IR spectra in KBr of the polycrystalline (bulk) sample and nanocrystalline $MnWO_4$ samples prepared by the hydrothermal method. (b) Mid-IR spectra in KBr of the polycrystalline (bulk) sample and nanocrystalline $MnWO_4$ samples prepared by coprecipitation method.

only to larger dielectric constant of KBr than nujol. Therefore, we attribute the observed shifts and broadening of bands in nujol to increased clumping since clumping may more easily occur when the powder is dispersed in nujol than in KBr [46].

Our results for the C-samples also show that the A_u modes, which are observed for polarization parallel to the b axis, absorb near LO and these bands shift closer to LO values with decreasing synthesis temperature (see Figs. 12c and 15). In contrast to this behavior, all B_u modes absorb slightly above TO or near TO, except of the 577 cm^{-1} B_u mode polarized along the c axis. Moreover, they exhibit negative shifts with decreasing synthesis temperature. This behavior is consistent with platelike shape of the particles, with b axis perpendicular to the plates, and decrease of the particle thickness with decreasing synthesis temperature. Different behavior is observed for the H-samples. For the H-220 sample all modes absorb near TO or slightly above TO. The only exception is the 838 cm^{-1} B_u stretching mode, which significantly shifts towards LO from its TO value equal to 795 cm^{-1} (see Fig. 15). When synthesis temperature decreases, the A_u modes shift towards LO and B_u modes towards TO values. This behavior is especially well visible for the H-150 and H-180 samples, which according to the SEM images are composed of nanorods and flowerlike microcrystals with narrow petals, respectively. It is worth to note that the band observed at 818 cm^{-1} for the polycrystalline sample shifts with decreasing particle size to higher wave numbers, i.e., 838 and 846 cm^{-1} for the H-220 and H-190 sample, respectively. However, with further decrease of the particle size this band shifts to lower wave numbers, i.e., 832 and 818 cm^{-1} for the H-180 and the H-150 sample, respectively. This result shows that the observed shift of the IR bands cannot be explained by change in the particle size only but it is closely related to shape of the particles and possibly also degree of their aggregation.

Another interesting feature of the recorded IR spectra is significant difference in intensity between some bands of the C- and H-samples. In the case of the C-samples, intensity of the A_u modes, which can be observed only for light polarized along the b axis, is significantly reduced. This behavior can most likely be attributed to platelike shape of the particles and maybe also to their preferential orientation with b axis perpendicular to the sample holder. In case of the H-samples, significant intensity reduction is observed for the bands near 800, 460, 210 and 150 cm^{-1}, which correspond to the B_u modes polarized along the a axis [37]. This result is consistent with SEM and XRD studies, which revealed that the crystallites often lay flat on the support with a axis normal to the surface. Finally, our spectra show appearance of a new band near 923 cm^{-1} for the C-400 and C-250 samples, which in analogy with similar Raman band at 920 cm^{-1} can be attributed to defects.

4. Conclusions

$MnWO_4$ nanoparticles were synthesized by two different methods, i.e. by surfactant-assisted hydrothermal method and annealing of a precursor obtained by precipitation from solution containing $MnCl_2$ and $Na_2WO_4 \cdot 2H_2O$. The obtained samples were characterized by XRD, SEM, TEM, Raman and IR methods. Our results show that the surfactant-assisted method with EA used as complexing agent leads to growth of flowerlike microcrystals composed of petals. These petals are hierarchically assembled by rodlike nanoparticles with the long axis along the c direction. Morphology and size of the crystallites change on the synthesis temperature. The second method leads to growth of strongly aggregated platelike crystallites.

Performed study shows that the Raman modes exhibited weak shifts in comparison with bulk $MnWO_4$ due to phonon confinement effect, strain and defects. Significantly different shifts observed for the H- and C-samples may also be related to different behavior of the $\delta = c - a$ parameter with the decreasing particle size, which results in different changes in the bond lengths and angles. Raman spectra also show that the B_g symmetry bands of the C-samples exhibited strong intensity decrease, which may be most likely attributed to creation of defects and some local structural changes.

In contrast to Raman-active modes, the IR-active modes showed pronounced changes in their wave numbers depending on the morphology and size of the crystallites. The observed shifts are correlated with magnitude of the LO–TO splitting, indicating that they are related mainly to the effect of long-range polarization. The most important conclusion from the IR studies is that one should be very careful when analyzing the IR data. For instance, the observed apparent coalescence of some IR bands may incorrectly be taken as an indication of a structural change into a more symmetric phase with decreasing particle size. It is also very often assumed that negative shift of an IR band with decreasing particle size can be attributed to phonon confinement effect or strain. However, our results show that such apparent

coalescence of bands and shifts towards lower wave numbers may have a completely different explanation. All these facts show that in order to understand the vibrational properties of a nanocrystalline material, it is essential at first to understand very well properties of bulk. In particular, it is very important to know symmetry of the observed modes and their polarization dependence.

References

[1] O. Heyer, N. Hollmann, S. Jodlauk, L. Bohaty, P. Becker, J.A. Mydosh, T. Lorenz, D. Khomskii, J. Phys. Condens. Matter 18 (2006) L471.
[2] A.H. Arkenbout, T.T.M. Palstra, T. Siegrist, T. Kimura, Phys. Rev. B 74 (2006) 184431.
[3] K. Taniguchi, N. Abe, T. Takenobu, Y. Iwasa, T. Arima, Phys. Rev. Lett. 97 (2006) 097203.
[4] L. Zhang, C. Lu, Y. Wang, Y. Cheng, Mater. Chem. Phys. 103 (2007) 433.
[5] W. Qu, J.U. Meyer, Meas. Sci. Technol. 8 (1997) 593.
[6] P. Becker, L. Bohaty, H.J. Eichler, H. Rhee, A.A. Kaminskii, Laser Phys. Lett. 4 (2007) 884.
[7] U. Kreibig, M. Vollmer, Optical Properties of Metal Clusters, Springer-Verlag, Berlin, 1995.
[8] K.Y. Lee, J.R. Lim, H. Rho, Y.J. Choi, K.J. Choi, J.G. Park, Appl. Phys. Lett. 91 (2007) 201901.
[9] R. Rao, A.M. Rao, B. Xu, J. Dong, S. Sharma, M.K. Sunkara, J. Appl. Phys. 98 (2005) 094312.
[10] L. Zhang, W. Wang, L. Zhou, H. Xu, Small 3 (2007) 1618.
[11] J.M. Weismann, H.B. Sunkara, A.S. Tse, S.A. Asher, Science 274 (1996) 959.
[12] S. Mann, Nat. Mater. 8 (2009) 781.
[13] W. Tong, L. Li, W. Hu, T. Yan, X. Guan, G. Li, J. Phys. Chem. C 114 (2010) 15298.
[14] S.J. Chen, X.T. Chen, Z. Xue, J.H. Zhou, J. Li, J.M. Hong, X.Z. You, J. Mater. Chem. 13 (2003) 1132.
[15] S. Lei, K. Tang, Z. Fang, Y. Huang, H. Zheng, Nanotechnology 16 (2005) 2407.
[16] W.B. Hu, X.L. Nie, Y.Zh. Mi, Mater. Charact. 61 (2010) 85.
[17] Y. Xing, S. Song, J. Feng, Y. Lei, M. Li, H. Zhang, Solid State Sci. 10 (2008) 1299.
[18] Y.X. Zhou, Q. Zhang, J.Y. Gong, S.H. Yu, J. Phys. Chem. C 112 (2008) 112.
[19] S. Thongtem, S. Wannapop, T. Thongtem, Trans. Nonferrous Met. Soc. China 19 (2009) s100.
[20] Powder diffraction diagram simulation program Poudrix V2, Jean Laugier and Bernard Bochu, ENSPG, Grenoble, France, 2001.
[21] J. Macavei, H. Schultz, Z. Kristallogr. 207 (1993) 193.
[22] J.I. Langford, A.J.C. Wilson, J. Appl. Cryst. 11 (1978) 102.
[23] M. Crosa, V. Boero, M. Franchini-Angela, Clays Clay Miner. 47 (1999) 742.
[24] S. Chattopadhyay, P. Ayyub, V.R. Palkar, M. Multani, Phys. Rev. B 52 (1995) 13177.
[25] J.M. Amigó, F.J. Serrano, M.A. Kojdecki, J. Bastida, V. Esteve, M.M. Reventós, F. Marti, J. Eur. Cer. Soc. 25 (1995) 1479.
[26] T.R. Anantharaman, J.W. Christian, Acta Cryst. 9 (1956) 479.
[27] N.C. Halder, C.N.J. Wagner, Acta Cryst. 20 (1966) 312.
[28] H.H. Tian, M. Atzmon, Phil. Magn. A 79 (1999) 1769.
[29] P. Ayyub, V.R. Palkar, S. Chattopadhyay, M. Multani, Phys. Rev. B 51 (1995) 6135.
[30] V.P. Sakhnenko, N.V. Ter-Oganessian, J. Phys. Condens. Matter 22 (2010) 226002.
[31] V.P. Sakhnenko, N.V. Ter-Oganessian, Ferroelectrics 410 (2010) 12.
[32] S.H. Yu, B. Liu, M.S. Mo, J.H. Huang, X.M. Liu, Y.T. Qian, Adv. Funct. Mater. 13 (2003) 639.
[33] B. Liu, S.H. Yu, L. Li, F. Zhang, Q. Zhang, M. Yoshimura, P. Shen, J. Phys. Chem. B 108 (2004) 2788.
[34] B. Ingham, C.V. Chong, J.L. Tallon, Curr. Appl. Phys. 6 (2006) 553.
[35] B. Ingham, C.V. Chong, J.L. Tallon, Soft condensed matter: new research, in: K.I. Dillon (Ed.), Organic–Inorganic Layered Hybrid Materials, Nova Science Publishers, 2007 (Chapter 6).
[36] M. Maczka, M. Ptak, K. Hermanowicz, A. Majchrowski, A. Pikul, J. Hanuza, Phys. Rev. B 83 (2011) 174439.
[37] J.E. Spanier, R.D. Robinson, F. Zhang, S.W. Chan, I.P. Herman, Phys. Rev. B 64 (2001) 245407.
[38] A.K. Arora, M. Rajalakshmi, T.R. Ravindran, V. Sivasubramanian, J. Raman Spectrosc. 38 (2007) 604.
[39] G. Gouadec, P. Colomban, Progr. Cryst. Growth Character. Mater. 53 (2007) 1.
[40] M. Saito, J. Suda, T. Sato, J. Spectrosc. Soc. Jpn. 51 (2002) 65.
[41] D. Errandonea, F.J. Manjon, N. Garro, P. Rodriguez-Hernandez, S. Radescu, A. Mujica, A. Munoz, C.Y. Tu, Phys. Rev. B 78 (2008) 054116.
[42] I.I. Shaganov, T.S. Perova, V.A. Melnikov, S.A. Dyakov, K. Berwick, J. Phys. Chem. C 114 (2010) 16071.
[43] Q. Zhang, Z. Zhang, Appl. Phys. A 91 (2008) 631.
[44] J.T. Luxon, D.J. Montgomery, R. Summitt, Phys. Rev. 188 (1969) 1345.
[45] K. Genzel, T.P. Martin, Phys. Status Solidi B 51 (1972) 91.
[46] M. Abdulkhadar, B. Thomas, Nanostruct. Mater. 5 (1995) 289.